# A grid-connected PV system based on quasi-Z-source inverter with maximum power extraction

Elmorshedy, Mahmoud F.; Essawy, Ihab Jamal Al; Rashad, Essam M.; Islam, Md Rabiul; Dabour, Sherif M.

*Published in:*
IEEE Transactions on Industry Applications

*DOI:*
10.1109/TIA.2023.3275557

*Publication date:*
2023

*Document Version*
Author accepted manuscript

# A Grid-Connected PV System Based on Quasi-Z-source Inverter with Maximum Power Extraction

Mahmoud F. Elmorshedy, *Member*, *IEEE*, Ihab Jamal Al Essawy, Essam M. Rashad, *Senior Member*, *IEEE*, and Md Rabiul Islam, *Senior Member, IEEE* Sherif M. Dabour, *Senior Member*, *IEEE*

***Abstract*—This paper proposes an approach to link photovoltaic arrays with the AC grid using Z-source inverter (ZSI) and quasi-Z-source inverter (QZSI) topologies. These topologies boost the DC-link voltage and invert it to AC voltage in one stage, resulting in a reduction in the overall system size and cost. The paper presents a control technique that fixes the DC-link voltage on the inverter bridge terminals, tracks the maximum power point (MPPT), and controls the amount and quality of power injected into the grid using unity power factor. The proposed control algorithm utilizes two independent control variables, shoot-through duty cycle (ST) and modulation index, to decouple the control of the DC and AC sides. The effectiveness of the proposed control technique is verified through simulations of a grid-connected PV system. The results demonstrate that the proposed system can efficiently extract maximum power from PV arrays while regulating the DC-link voltage and ensuring unity power factor operation. Additionally, experimental testing of ZSI/QZSI further confirms the results of analysis and simulation.**

***Index Terms*—Photovoltaic, Z-source inverter, grid connected, standalone, maximum power point tracking, decoupling control, unity power factor.**

## I. Introduction

RENEWABLE energy sources (RESs) offer numerous advantages over traditional sources [1-4]. Photovoltaic (PV), wind, and biomass systems are some examples of RESs. Recently, PV energy has gained popularity worldwide due to its low cost and increased utility [5]. Grid-connected PV systems are an optimal solution to reduce production costs [3]. The generated PV power is transmitted to the utility grid via a centralized inverter or multiple small inverters connected to individual PV modules [4]. To ensure power system stability and quality, extensive research has focused on controlling grid-connected PV systems to enhance their performance.

Manuscript received July 2nd, 2022; revised January 5th, 2023;

Mahmoud F. Elmorshedy (Corresponding Author), Ihab Jamal Al Essawy, Sherif M. Dabour, and Essam M. Rashad are all with the Department of Electrical Power and Machines Engineering, Faculty of Engineering, Tanta University, Egypt. (e-mails: mahmoud.elmorshedy@f-eng.tanta.edu.eg; ehab.gamal78.en@gmail.com, sherif.dabour@f-eng.tanta.edu.eg, emrashad@ieee.org). Sherif Dabour is also with Glasgow Caledonian University, UK (sherif.dabour@gcu.ac.uk).

M. R. Islam is with the School of Electrical, Computer and Telecommunications Engineering, University of Wollongong, NSW 2522, Australia (e-mail: mrislam@uow.edu.au, rabiulbd@hotmail.com).

Grid-connected PV systems commonly use voltage source inverters (VSIs), but it has drawbacks such as:

a) the grid voltage must be lower than PV voltage due to the VSI's buck inverter nature in DC to AC conversion,
b) simultaneous activation of both switches in a phase can result in shoot-through (ST) and damage to the bridge, and
c) the use of dead time to prevent ST can cause distortion in the output current [4].

To address the inherent buck inverter nature, a common approach is to utilize a two-stage conversion system. A typical two-stage conversion process utilized in grid-connected PV systems [5]. The first stage uses a DC-to-DC converter, which is usually incorporates a boost or buck-boost converter to control the PV output voltage and extract the maximum power. The second stage involves a voltage source inverter (VSI) that converts DC to AC power. While the two-stage configurations have been successful, they suffer from drawbacks such as increased device count, low efficiency, low reliability, high cost, and large size [5,6].

Conversely, the single-stage topology has emerged to overcome the drawbacks of two-stage configurations. One such topology is the impedance-source inverter (ZSI), which uses a Z-source impedance network to connect the inverter power circuit to the PV source. The ZSI, shown in Fig. 1(a), has been widely discussed in literature [5-7]. However, it has some shortcomings, which led researchers to modify or add passive components to the impedance network to address these issues. One of the most popular topologies resulting from this research is the quasi-Z-source inverter (QZSI), shown in Fig. 1(b). This paper firstly reviews the composition and working principle of the QZSI and clarifies the advantages and disadvantages of both the ZSI and QZSI.

The ST duty cycle control in both ZSI and QZSI enables the boosting of DC-link voltage while eliminating dead time, thereby reducing total harmonic distortion (THD) in the output and improving power quality. During the last few years, ZSI is utilized in various applications such as adjustable speed drive and power conversion systems from a constant DC voltage source, whereas QZSI is preferred for use in PV systems [?]. These inverters are controlled by two independent variables, namely the ST duty ratio ($D_o$) and the modulation index ($m$). A simple boost pulse width modulation (SBPWM) strategy is employed to drive the inverter bridge [?].

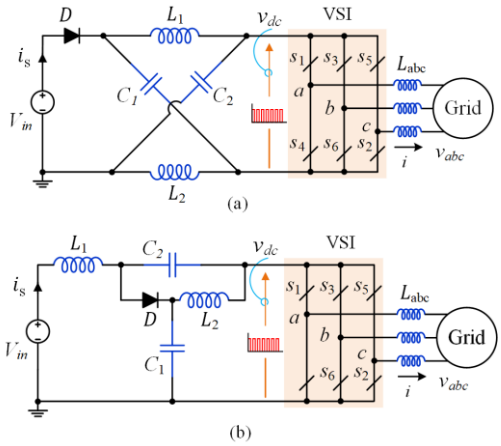


Fig. 1. Single state inverter (a) ZSI and (b) QZSI.

Generally, PWM methods aim to convert null states into ST states and maintain the active interval states, preventing circuit devices from being damaged due to short circuit or faulty switching. This results in an improved inverter with significantly increased reliability.

This paper focuses on using QZSI to connect PV arrays to the grid and proposes a comprehensive control technology to achieve MPPT and regulate the DC-link voltage. The control strategy begins with using the P&O algorithm to achieve MPPT of the PV array. The PI controller determines the ST duty ratio and regulates the DC-link voltage while providing the $d$-axis synchronous current reference frame. The presented control strategy can achieve unity power factor and transfer the maximum available power to the grid under various radiation levels. The effectiveness of the control technique is verified through simulations conducted in MATLAB/Simulink, and the operation principle and characteristics of QZSI are verified through experimental testing.

The paper is structured as follows: first, the proposed system structure is presented, followed by an analysis of the QZSI operating principle and PWM strategy in Section II. Section III discusses the MPPT algorithm and control for both DC and AC sides. In Section IV, the LC-filter design and PI tuning for the proposed system are analysed. Section V presents simulation and experimental results with a discussion. Finally, the conclusion of the presented work is summarized in Section VI.

## II. Overall System Configuration

Figure 2 shows the scheme diagram of the proposed system. The system contains a five main parts: PV panels, QZSI, filter, utility grid, and control unit. The control system comprises three control units: MPPT unit, outer control loop unit, and inner control loop unit [3,6,8,13].

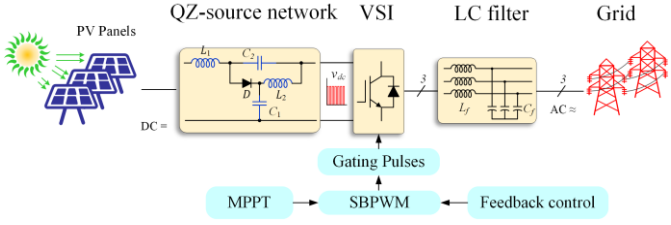


Fig. 1. The grid-connected PV system depend on ZS network circuit diagram.

### A. Operating principles of the QZSI

A QZSI equivalent circuit is slightly different from a ZSI equivalent circuit as shown in Fig. 1. For mathematical derivation, a parallel switch $S_p$ is used to represent the VSI as illustrated in Fig. 3. During the ON state of $S_p$, the DC-link terminals are shorted (ST mode) as shown in Fig. 4, On the other side, if the $S_p$ is in OFF state, the impedance network is connected to the load (active or null state) as shown in Fig. 5, it is called (non-ST mode) where the diode can be expressed by the $S_d$ series switch. The steady-state analysis of the QZSI is performed under the following assumption [3].

- The two inductors and capacitors are selected so that: $L_1$=$L_2$=L & $C_1$=$C_2$=C.
- Semiconductor switches are considered ideal.
- The internal resistances of inductors, capacitors and semiconductor switches are neglected.
- Passive elements like Inductors and capacitors, also the resistors are linear, stable over time, and independent of frequency.
- Choosing the appropriate size of inductance and capacitance to reduce the dc ripples.

The QZSI operates in two modes, ST mode, and non-ST mode. The performance of ZSI can be analyzed as follows.

#### 1) ST-state

The equivalent circuit of the ST state is seen in Fig. 4. This state occurs when any of the seven ST states shorts the impedance network terminals; in another meaning, the quasi-Z-source network (QZSN) is shorted by connecting both switches in any leg of the bridge simultaneously. In ST states, the circuit can be represented as follows [3].

$$V_L = V_c \quad (1)$$

$$V_d = V_{in} - 2V_c \quad (2)$$

$$I_c = -I_L \quad (3)$$

$$I_{dc} = 2I_L \quad (4)$$

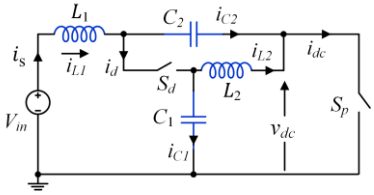


Fig. 3 The equivalent circuit of the QZSI.

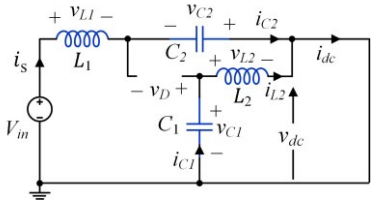


Fig. 4 The equivalent circuit of the QZSI at ST state.

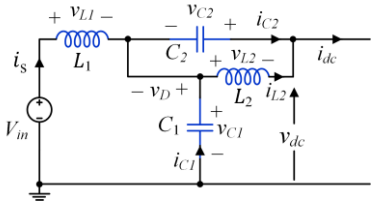


Fig. 5 The equivalent circuit of the QZSI at non-ST state.

*2) Non-ST- state*

The equivalent circuit of the non-ST state is illustrated in Fig. 5, where the inverter operates in one of the active or null states (such as a conventional VSI) for a period of total active time, $T_1$. It is noticeable that the diode is forward biased, and the capacitors begin to charge, and then the previously stocked power in the inductors is transferred to the load. The mathematical representation of this case is as follows [1]:

$$V_L = V_{in} - V_c \quad (5)$$

$$V_d = 0 \quad (6)$$

$$V_{dc} = 2V_c - V_{in} \quad (7)$$

$$I_c = I_L - I_{dc} \quad (8)$$

$$I_c = I_s - I_L \quad (9)$$

The overall interval of the shoot-through time is $T_0$ while $T_1$ is the total active time.

In the stable case, the average voltage $V_{L1}$ over the switching time T should be zero [2], which results in the following equations:

$$V_L = \frac{1}{T}\int_0^T V_L\ (t)dt = \frac{T_\circ V_c + T_1(V_{in} - V_c)}{T} = 0 \quad (10)$$

Suppose $D_o$ is the ST duty cycle and using Eqn. (3.13), the relation between the capacitor voltage and the input voltage can be deduced as follows:

$$\frac{V_c}{V_{in}} = \frac{T_1}{T_1 - T_\circ} = \frac{1 - D_\circ}{1 - 2D_\circ} \quad (11)$$

Also, the average DC-link voltage ($V_{dc}$) at the input of the inverter can be decided and concluded as follows:

$$V_{dc} = \frac{1}{T}\int_0^T V_{dc}\ (t)dt = \frac{T_\circ 0 + T_1(2V_c - V_{in})}{T} = V_{in}\,T_1/(T_1 - T_\circ) \quad (12)$$

while the peak value of the chopping DC-link voltage ($v_{dc}$) across the inverter bridge can be deduced as follows:

$$v_{dc} = 2V_c - V_{in} = \frac{T}{T_1 - T_\circ}V_{in} = BV_{in} \quad (13)$$

where B is the boost factor resulting from the ST state and can be deduced as follows:

$$B = \frac{T}{T_1 - T_\circ} = \frac{1}{1 - 2\frac{T_\circ}{T}} = \frac{1}{1 - 2D_\circ} \quad (14)$$

Since the value of $D_o$ is larger than zero and less than 0.5, the value of $B$ is larger than one, and $D_o$ can be expressed in terms of $B$ as follows:

$$D_o = T_\circ/T = (B - 1)/(2B) \quad (15)$$

$$1 - T_\circ/T = (B + 1)/(2B) \quad (16)$$

From (11) and (16) the capacitor voltage can be deduced as follows:

$$V_c = V_{in}\,(B + 1)/2 \quad (17)$$

The second prime difference between ZSI and QZSI is that the capacitor voltage on $C_2$ is significantly reduced compared to $C_1$, so the voltages on the capacitors compared to the QZSI can be expressed as follows:

$$V_{c1} = \frac{1 - D_\circ}{1 - 2D_\circ}BV_{in} = \frac{B + 1}{2}V_{in} \quad (18)$$

$$V_{c2} = BV_{in}\ D_\circ/(1 - 2D_\circ) \quad (19)$$

Substituting the value of the input source voltage from (13) into (18) the peak value of the DC-link voltage can be deduced as follows:

$$V_{dc} = BV_{in} = \frac{2V_c}{B + 1}B = \frac{2B}{B + 1}V_c \quad (20)$$

The peak value of the output phase voltage ($v_{ac}$) can be deduced as follows:

$$v_{ac} = MV_{dc}/2 = MBV_{in}/2 \quad (21)$$

where $m$ is the modulation index and offset by (20) in (21). The output ac voltage of the inverter can be formulated as follows:

$$v_{ac} = GV_{in}/2 \quad (22)$$

where $G$ is the ZSI gain can be formulated as follows:

$$G = MB \quad (23)$$

whereas $B$ is the gain of the impedance network and $m$ is the gain of the VSI, the voltage transfer ratio can be formulated as follows:

$$VTR = v_{ac}/V_{in} = G/2 \quad (24)$$

For a conventional VSI, it is known that the peak value of the output phase voltage is $v_{ac} = MV_{in}/2$. But in ZSI/QZSI and according to (21), the presence of an added multiplication factor of $B$ gives the boosting ability in ZSI/QZSI compared to the voltage conversion ratio of VSI. But realistically, the non-ideal values or the internal resistance of the switches and passive components affects the value of $B$. The duty cycle of the ST state over the non-ST states of the inverter can be used to control the boost factor $B$. The PWM control of the inverter is unaffected by the ST state as it produces zero voltage only across the load as it is during zero states.

Similarly, the average value of the current passing through the capacitor over the entire switching period is zero [6]. Also, the average value of $I_{dc}$ over the non-ST period is constant. So, using (3), (8), the inductor current can be formulated as follows:

$$I_L = I_{dc}\ (1 - D_\circ)/(1 - 2D_\circ) \quad (25)$$

Also, the input current $I_{in}$ through non-ST mode can be formulated as follows:

$$I_{in} = I_L/(1 - D_\circ) \quad (26)$$

## III. Control Strategy For The Proposed System

In this section, the details of each control objective will be presented in detail.

### *A. MPPT Control Techniques*

There are many MPPT algorithms used to extract all available energy in the PV array [5]. The perturbation and observation (P&O) diagram of the MPPT control is shown in Fig. 6. This technique is commonly used due to its simplicity. The output of the MPPT algorithm is in the form of two reference lines, $V_p$ and $V_n$, which define the ST period. The PWM technology is fed by these two lines as shown in Fig. 7. Thus, the DC-link voltage can be increased according to the ST intervals. Hence, the DC-link voltage can be boosted according to the ST periods. From (10), and according to the relation between the PV array voltage and the $V_C$, controlling the $V_{C2}$ of

the ZSI leads to adjusting the voltage of the PV array. The Z-source DC-link voltage, $V_{dc}$ is optimized to equal the PV voltage at the maximum power point. This can only be happened by simultaneous operation of every phase leg switches in inverter bridge [9].

The P&O method compares the output power of the PV array at the previous step with the output power of the new step. This may result in increasing or decreasing the array voltage until the difference between the power of the previous and new steps reaches zero. Therefore, the value of the reference voltage changes with a fixed value. Operating point is moving on the MPP curve because of repeatedly rising or lessening the array voltage as shown in Fig. 8. This figure shows that increasing or decreasing the voltage value will change the amount of power directly. Therefore, if there is an increase in power, the subsequent perturbation must remain in the same direction to achieve MPP. If there is a reduction in power, the direction of the perturbation must be reversed. Fig. 9., shows the practical algorithm of MPPT based on P&O.

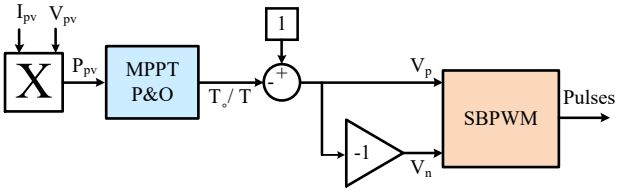


Fig. 6. The block diagram of the MPPT based on the P&O.

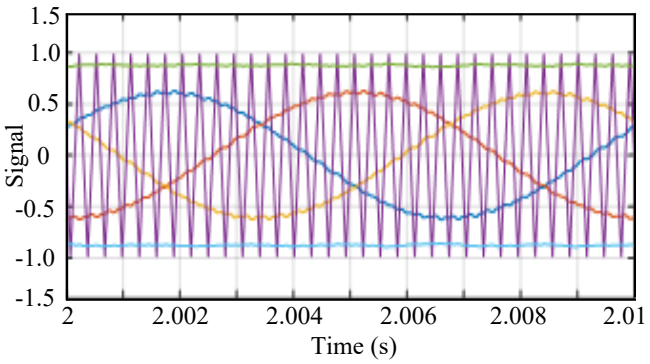


Fig. 7. Description of the SBPWM.

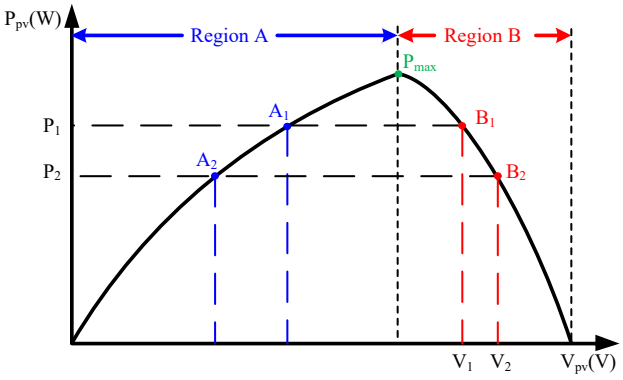


Fig. 8. Operation principle of P&O MPPT algorithm.

### B. *Control principle of grid-connected PV system*

The controlling of a grid-connected PV system is aimed to convert the DC power to AC power matches the grid requirements. The inner current control loop is designed to achieve the unity power factor. Meanwhile, the external voltage control loop is used to ensure that the inverter voltages can follow the AC grid voltage. The PV voltage is further controlled by the ST duty cycle to track the MPP [3]. The general circuit diagram of a three-phase QZSI connected to a PV with a control structure is shown Fig. 10. The main purpose of this control strategy is to maintain a unity power factor and reducing THD.

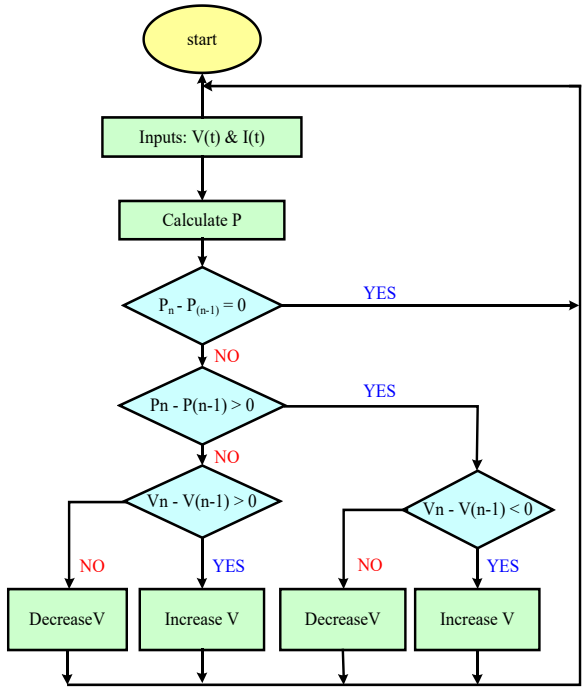


Fig. 9. Flow chart of Perturb & Observe technique for the MPPT.

The control strategy of ZSI/QZSI in the grid-connected PV system is shown in Fig. 11., which is split into DC section control and AC section control. The DC controller provides a fixed average DC-link voltage from a chopped DC output to the inverter. On the other hand, the AC side is controlled in the synchronous $dq$ frame. The output signal from DC-link voltage control serves as the reference value of $d$-axis.

Meanwhile, the reference current for the $q$-axis is considered zero to realize unity power factor. The $dq$-axis current signals are controlled to achieve the modulating signal then they are converted to the three-phase sinusoidal reference voltage signal in (a, b, c) frame. By adopting the SB-PWM the active and null states are produced for control ZSI bridge. Three-phase sinusoidal reference signals are available with the help of the current control loop with the aided of phase angle, $\omega t$ and voltages and currents in $dq$ frame of the reference modulation index, $m$ [5].

More analysis about the current control loop for QZSI in the synchronous reference frame can be expressed by:

$$V_d = \left(Ri_d + L\left(\frac{di_d}{dt}\right) + \omega L i_q + e_d\right) \tag{27}$$

$$V_q = \left(Ri_q + L\left(\frac{di_q}{dt}\right) - \omega L i_d + e_q\right) \quad (28)$$

where $R$ and $L$ are the line filter resistance and inductance, respectively, $e_d$ and $e_q$ are the transformed grid voltages and $\omega$ is the angular frequency of the grid.

Re-writing (17) and (18):

$$V_d = \left(\Delta v_d + \omega L i_q + e_d\right) \quad (29)$$

$$V_q = \left(\Delta v_q - \omega L i_d + e_q\right) \quad (30)$$

where

$$\Delta v_d = Ri_d + L\, di_d/dt \quad (31)$$

$$\Delta v_q = Ri_q + L\, di_q/dt \quad (32)$$

Since the coupling terms ($\omega L i_d$ and $\omega L i_q$) and the grid voltages (ed and eq) are known, the current inner loop control must determine the voltage drop on the filter impedances ($\Delta v_d$ and $\Delta v_q$) to achieve the current references $I_{dref}$ and $I_{qref}$. The schematic diagram of the current control depends on (21) and (22) is depicted in Fig. 12 [8]. Also, phase-locked-loop control technique is used to control the phase angle and frequency between the inverter's current and the grid voltage. Fig. 13., shows the phase-locked loop, (PLL) technique for the grid interconnection [10].

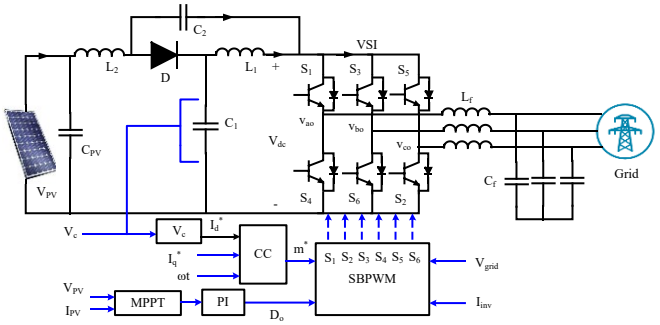


Fig. 10. The PV-based three-phase QZSI with the control structure.

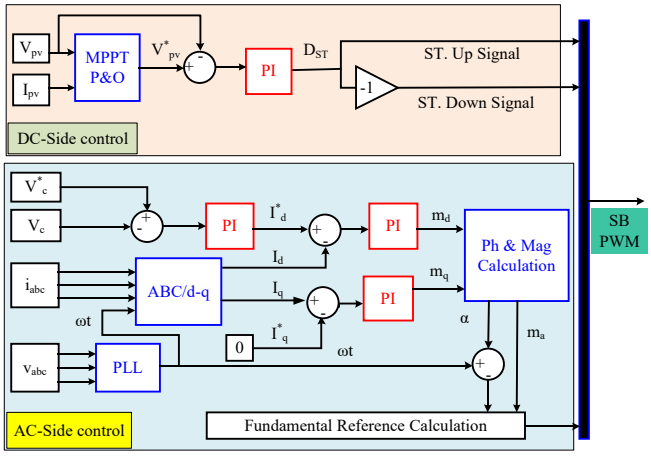


Fig. 11. Control technique for ZSI/QZSI in a grid-connected PV system.

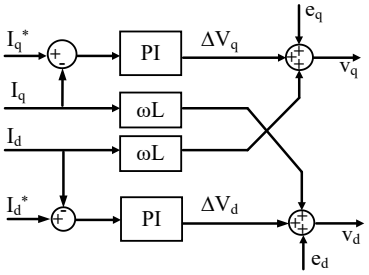


Fig. 12. Control diagram of the current control loop.

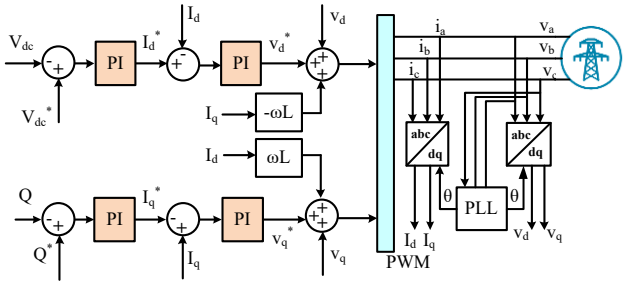


Fig. 13. Block diagram of the grid side inverter including three-phase PLL.

## IV. LC-Filter Design and PI Tuning

The filter is an important device to be inserted between the inverter and the grid in order to avoid parallel resonance, to meet imposed utility distortion limits, and improve the poor power quality. The harmonic currents injected by a grid connected inverter can be classified as [22]

- Low frequency harmonics,
- Switching frequency harmonics, and
- High frequency harmonics

Each frequency must be attenuated sufficiently and appropriately. L-filter (first order), LC-filter (second order), and LCL-filter are the three main harmonic filter topologies. (third order). Each topology has a different range of attenuation. Because of their smaller component dimensions, LCL-filters are becoming more popular. Meanwhile, the main disadvantage of the LCL-filter is the instability caused by the resonance of the filter elements, which necessitates some form of damping. Determining the electrical parameters of (LCL) inductance and capacitance is also a difficult task. LCL-filter design methodologies are difficult due to the standard's harmonic injection limit. As a result, the LC-filter shown in Fig. 2 is used in this work. The filter inductor, $L_f$, is chosen based on the maximum allowable ripple current in the inverter switching devices. In order to limit the reactive voltage drop and the required DC link voltage value, the reactance should be less than 10% of the system's base impedance.

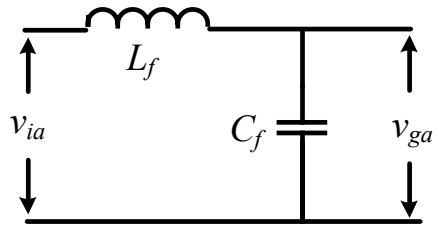


Fig. 14 The adopted LC-filter.

To determine the maximum inductor ripple current, the values of via and $v_{ga}$ are given by

$$v_{ia} = \frac{2}{3}V_{dc} \quad (33)$$

$$v_{ga} = \frac{1}{3}V_{dc} \quad (34)$$

The voltage across the inductor is given by

$$v_{Lf} = L_f \frac{\Delta i_{Lf}}{\delta T_s} = v_{ia} - v_{ga} = \frac{1}{6}V_{dc} \quad (35)$$

$$L_f \frac{\Delta i_{Lf}}{\delta T_s} = \frac{1}{6}V_{dc} \quad (36)$$

From the previous equation, the filter inductor value can be calculated by

$$L_f = \frac{\delta V_{dc}}{6 f_s \Delta i_{Lf}} \quad (37)$$

where $V_{dc}$ is the dc-link voltage, $f_s$ the switching frequency, $\Delta i_{Lf}$ the allowable percentage of ripple current, and $\delta$ the maximum duty cycle.

Meanwhile, the filter capacitor's maximum value, $C_f$, is determined by the acceptable PF reduction at the rated power. As a result, the maximum total capacitance of a given PF should be calculated, with approximately 30% of this capacitance reserved for the filter capacitor, $C_f$. This lower ratio is due to the fact that one of the capacitors in the other circuit may have a higher capacitor value. To reduce the first harmonic switching component and higher-order components, the minimum value of the principal capacitance is set to the output voltage ripple value. As a result, a sufficient margin must be allowed to calculate the size of the $C_f$ [23].

The tuning values of the PI controller-based voltage-oriented control are developed from equations (27) to (32) based on the filter values, where the d- and q- axis currents can be controlled by controlling the inverter d- and q- axis voltages $V_d$ and $V_q$. For the unity PF, the reference current $i_q^*$ is set to zero, while the $i_d^*$ is determined by the dc-link voltage controller. The errors generate the command voltage signals $v_d^*$ and $v_q^*$ via PI controllers, which are then transformed back to $v_{abc}^*$ using the grid space vector angle obtained by the phase-locked loop. (PLL). However, compensating signals, as shown in Fig. 6, are used to eliminate the coupling effect introduced in equations (27) and (28) respectively. After Taking Laplace Transform for (31) and (32), the above equations can be rewritten in the following forms

$$G_d(s) = \frac{i_d(s)}{\Delta v_d(s)} = \frac{1}{R + Ls} \quad (38)$$

$$G_q(s) = \frac{i_q(s)}{\Delta v_q(s)} = \frac{1}{R + Ls} \quad (39)$$

## V. Simulation and Experimental Test

In order to verify the effectiveness of the QZSI with the control techniques, a comparison between both QZSI and ZSI is presented. The simulation and experimental results are investigated based on MATLAB/Simulink model and prototype test platform of QZSI and ZSI. All data and parameters related to proposed system for simulation and experimental results are listed in Table I and Table II respectively. In order to obtain a fair comparison, the two converters with the control techniques are tested under the same load conditions, and the same switching frequency of 5 KHz for both experimentation and simulation results. The frequency is unified between because the highest frequency that the inductor used in the impedance network can withstand is 5 KHz.

### A. Simulation Results

The system model was simulated in a MATLAB/Simulink environment. To evaluate the results of the control scheme, the electrical parameters of the designed system are shown in Table 1. The values of the inductors and capacitors of the ZSI and QZSI networks are calculated depend on the design consideration of [9]. The current controller gains are set at $K_p = 0.3$ and $K_i = 100$. Meanwhile, gains of the DC-link voltage controller are -0.005 and -0.83. The response of the voltage controller is after the response of the inner current control loop to avoid any coupling of ST duty ratio, Do and modulation index, $m$. The DC-link voltage reference can be calculated from [24]:

$$1 > V_{dc}(per\ unit) \geq 1 - m \quad (29)$$

The peak amplitude of the output can be expressed as:

$$V_{ac} = \left(\frac{m}{2m-1}\right) \quad (30)$$

From (11), If $V_{pv} = 492V$ and $m = 0.8$ so that $v_{ac} = 240V$. Meanwhile, from (10) $V_{dcref} = 630V$ which achieves (24).

The overall system performance is tested under different irradiance levels where the solar insolation is reduced from 1000 W/m$^2$ to 200 W/m2 at 0.7 s and then increased to 1000 W/m2 at 1.5 s. The effect of the MPPT is shown in Fig. 15. (a), in QZSI and in Fig. 5. (b), for ZSI. Figure 16., shows that the DC-link voltage remains constant in both QZSI/ZSI by the adopted control technique. It is closed to the DC reference voltage at all irradiation levels. In Fig. 17, the $V_{c1}$ is smaller than $V_{c2}$ in QZSI unlike ZSI in which the voltages of the two capacitors are equal. In Fig. 18, the unity power factor control is shown, the network voltage and the inverter current being in phase with each other. In Fig. 19, the three phases grid voltage with 120$^o$ phase shift is shown. Fig. 20, shows the three phases inverter current with 120$^o$ phase shift. The grid current has low distortion and is THD for current as shown in Fig. 21. Finally, Fig. 22, shows the injected power into the grid, which is equal to 21.5 kW.

TABLE I Simulation Specifications of the Proposed System

| No. | Symbol | Value | Unit |
|---|---|---|---|
| 1 | *Open-circuit voltage,* $V_{oc}$ | 64.2 | V |
| 2 | *Short circuit current,* $I_{sc}$ | 5.96 | A |
| 3 | *Switching frequency,* $F_s$ | 5000 | Hz |
| 4 | *Inductors of ZSN,* $L_1$&$L_2$ | 1000 | µH |
| 5 | *Capacitors of ZSN,* $C_1$&$C_2$ | 1000 | µF |
| 6 | *Filter,* $L_f$, $C_f$, $R_f$ | 5, 10, 0.05 | mH, µF, Ω |

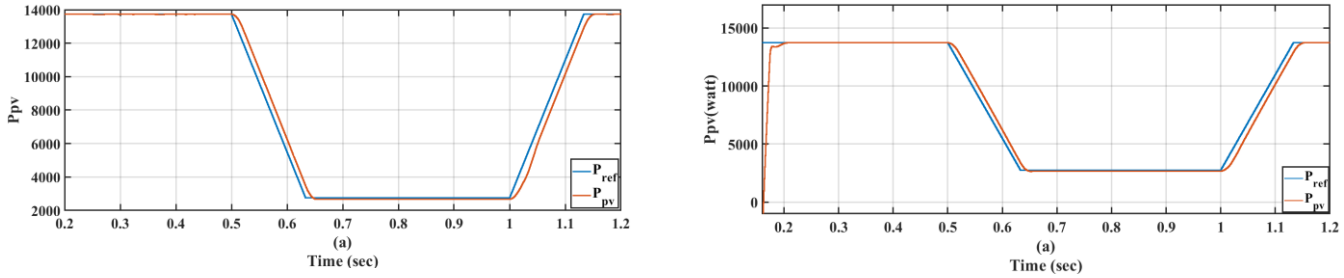


Fig. 15. PV array power compared with reference maximum power, a) QZSI, b) ZSI

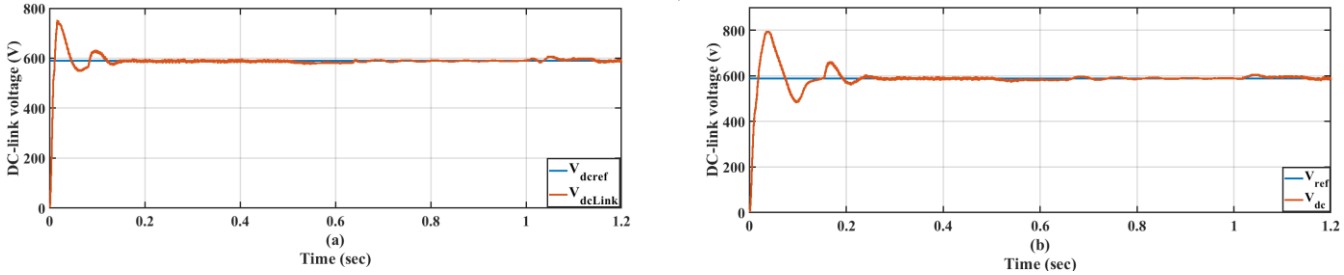


Fig. 16. The DC-link voltage compared to the reference DC voltage, a) QZSI, b) ZSI

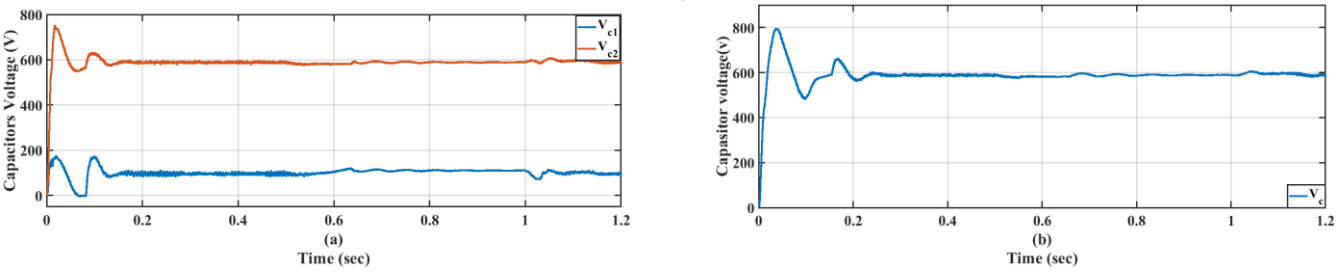


Fig. 17. The capacitor voltage, a) QZSI, b) ZSI

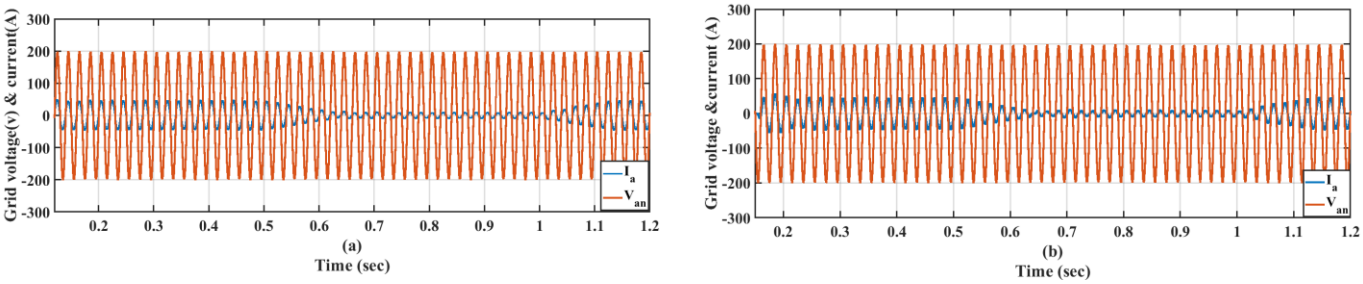


Fig. 18. Inverter output current with grid voltage, a) QZSI, b) ZSI

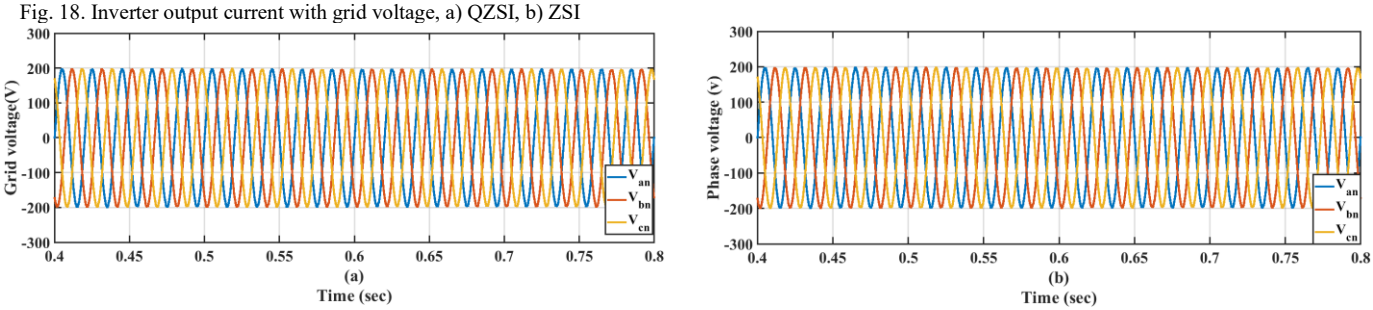


Fig. 19. Grid voltage with 120o phase shift, a) QZSI, b) ZSI

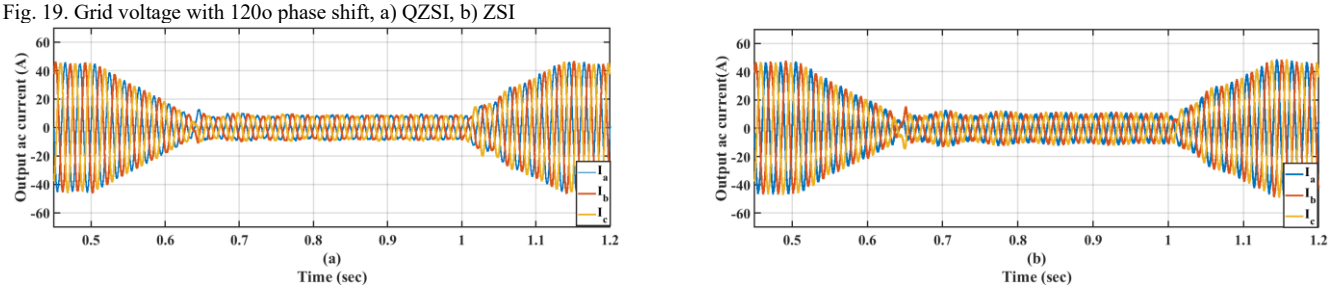


Fig. 20. Inverter output current, a) QZSI, b) ZSI

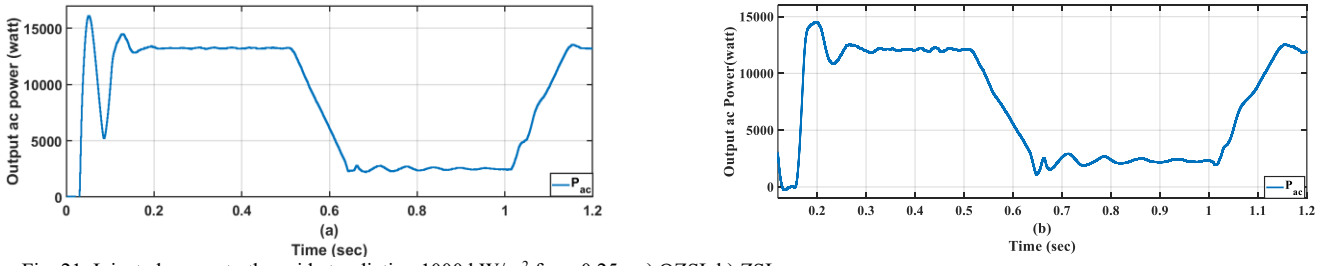


Fig. 21. Injected power to the grid at radiation 1000 kW/m$^2$ from 0.25s, a) QZSI, b) ZSI

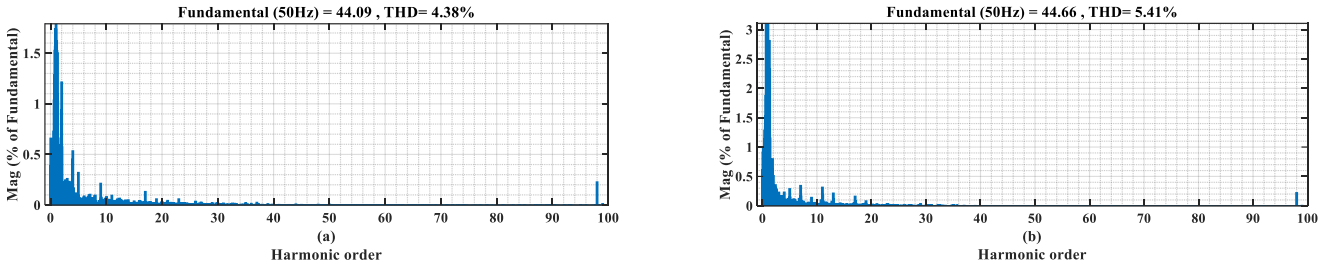


Fig. 22. THD for the grid current, a) QZSI, b) ZSI

### *B. Experimental Results*

Figure 23 shows the photograph of the experimental test platform. The experimental results are presented for prototype ZSI/QZSI based on the listed experimental parameters given in Table 2. In this case, the modulation index is set at $m = 0.7$ and then it is changed to 0.75. Hence, the ST duty ratio is $D_o = 0.3$ and changed to 0.25 in open-loop condition. Both QZSI and ZSI are verified and tested under the same operating conditions.

The QZSI experimental results are presented in Fig .24. Firstly, Fig .24(a) shows the DC-link voltage which begins with value reaches 90V and then drops to 73V due to the decrease in the value of $D_o$. Also, in the same figure a discontinuous current is shown. Fig. 24(b), shows the difference between $V_{c1}$ and $V_{c2}$. Fig. 24(c), shows a zooming of DC-link voltage signal. Meanwhile, Fig. 24(d) shows the continuous input current drawn from supply. It can be noticed that the input current has high ripples due to the DC source is converted from the AC source and hence it contains distortions, the inductor which used in the impedance network on the experimental test is not a high frequency inductor, and a simple boost pulse-width modulation method was used in the inverter control. BPWM uses fixed shoot-through times, which results in the appearance of low-frequency ripples on the current inductors of the impedance network. Fig. 24. (e) shows the sinusoidal load current in phase with output voltage. and two phases sinusoidal output voltage with 120º Phase shift. Fig. 24. (f, g) show the Spectrum for Load current and phase voltage.

ZSI results: Fig .25. (a), shows the DC-link voltage begins with value reaches 90V and then drops to 73V due to the decrease in the value of Do. Also, in the same figure a discontinuous current is shown. Fig. 25. (b), shows the difference between Vc1 and Vc2. Fig. 25. (c), shows a zooming of DC-link voltage signal, Fig. 25. (d). shows the continuous input current drawn from supply. Fig. 25. (e) shows the sinusoidal load current in phase with output voltage. and two phases sinusoidal output voltage with 120o Phase shift. Fig. 25. (f, g) show the Spectrum for Load current and phase voltage.

TABLE II. EXPERIMENTAL SPECIFICATIONS OF THE PROPOSED SYSTEM

| No. | Symbol | Value | Unit |
|---|---|---|---|
| 1 | *Input voltage,* $V_{in}$ | 30 | V |
| 2 | *Resistive Load,* $R_{load}$ | 20 | Ω |
| 3 | *Switching frequency,* $F_s$ | 5000 | Hz |
| 4 | *Inductors of ZSN,* $L_1$ &$L_2$ | 1, 0.9 | mH, Ω |
| 5 | *Capacitors of ZSN,* $C_1$ &$C_2$ | 470 | μ F |
| 6 | *Filter,* $L_f$, $R_f$ | 5, 0.05 | mH, Ω |

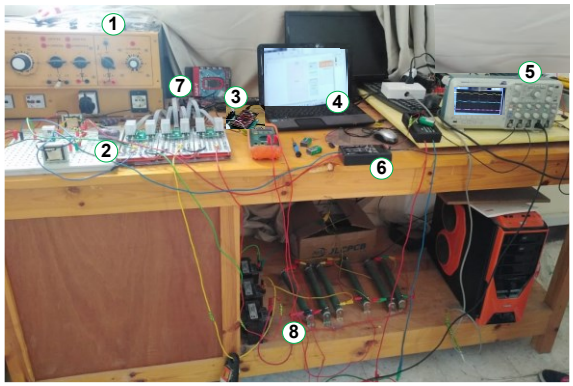


Fig. 23. Photograph of the overall experimental setup. ① DL1013M2 power supply module, ② QZS dc-link side, ③ LAUNCHXL-F28379D kit, ④ Laptop, ⑤ Oscilloscope, ⑥ Voltage measurements board, ⑦ Three-phase inverter bridge with current sensors, ⑧ RL load.

## VI. CONCLUSION

Based on the presented study, further scrutiny is needed for the use of QZSI and ZSI in connecting PV systems to the grid. The study proposes a separate control scheme for the photovoltaic system, which achieves three objectives: 1) producing the maximum available power in the solar panel, 2) regulating the DC link voltage, and 3) ensuring a unity power factor grid operation. The study analyzes the QZSI operating principles with control systems and implements a MATLAB/Simulink model to test both QZSI and ZSI-based PV systems. The

simulation results prove the correctness of the QZSI operating principle and demonstrate the possibility of improving the performance of the grid-connected PV system. The model achieves some QZSI targets, such as reducing the output THD, but it suffers from high ripples in the DC-link voltage and a small modulation area. Experimental results confirm the advantages of QZSI in terms of voltage boosting and overcoming the problems of traditional ZSI, such as discontinuous input current and high inrush current.

(a)

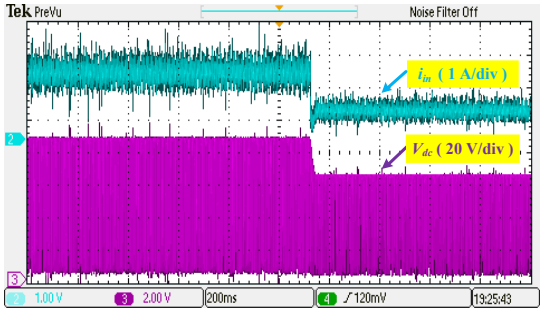


*T* ( 200 ms/div )

(b)

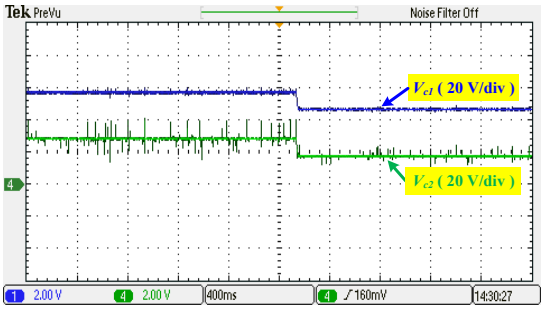


*T* ( 400 ms/div )

(c)

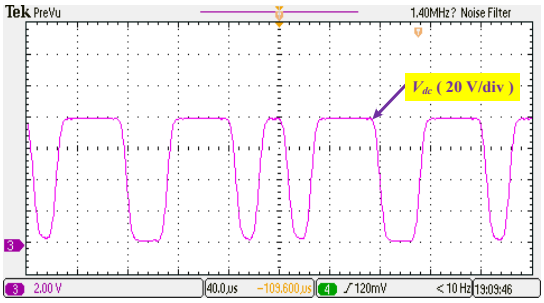


*T* ( 40 ms/div )

(d)

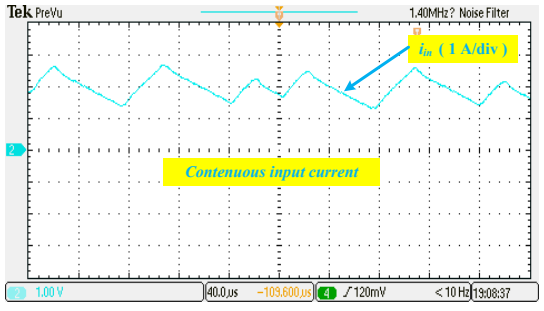


*T* ( 40 ms/div )

(e)

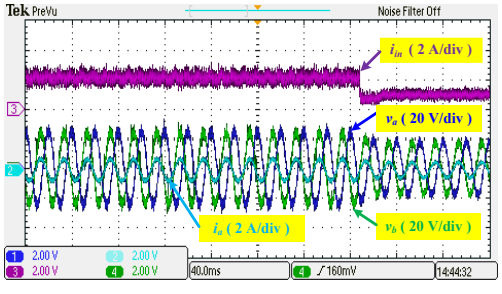


*T* ( 40 ms/div )

(a)

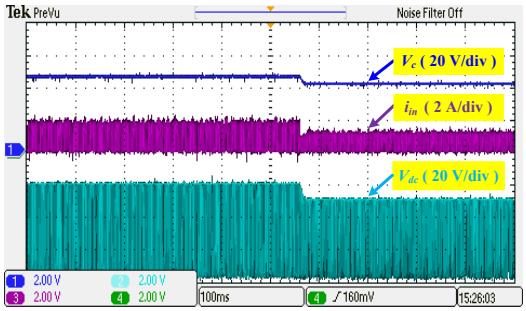


*T* ( 100 ms/div )

(b)

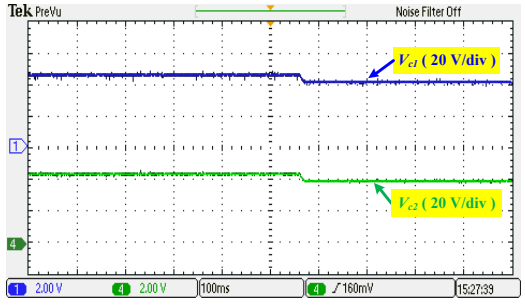


*T* ( 100 ms/div )

(c)

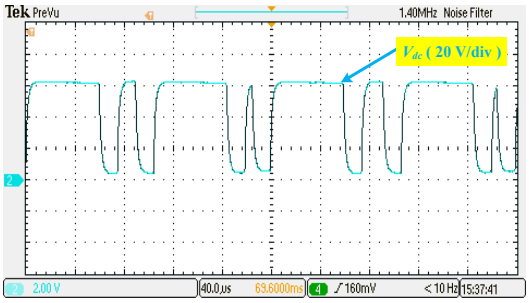


*T* ( 40 ms/div )

(d)

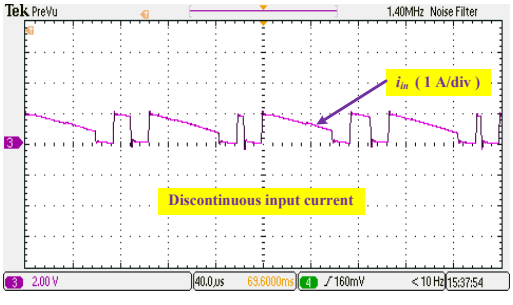


*T* ( 40 ms/div )

(e)

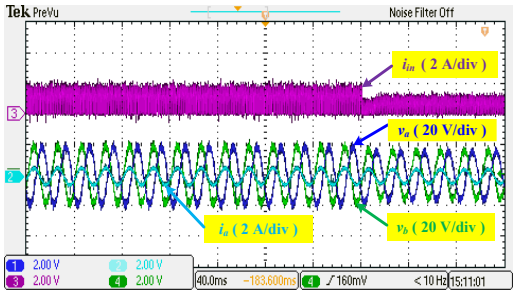


*T* ( 40 ms/div )

(f)

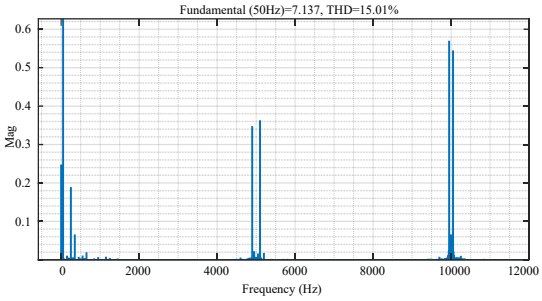


(g)

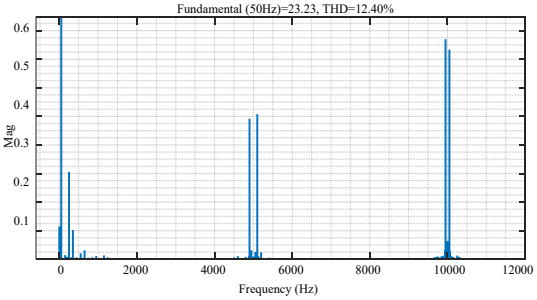


Fig. 24. Experimental results for QZSI. a) DC-link voltage, and Input current, b) capacitor voltage, c) Zooming of DC-link voltage, d) Zooming of input current, e) Zooming of load current with two phase ac voltage, f) THD in current, g) THD in voltage.

(f)

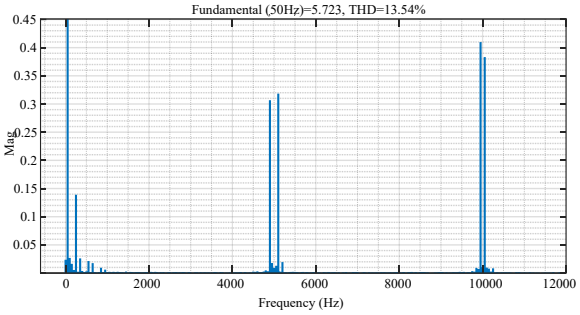


(g)

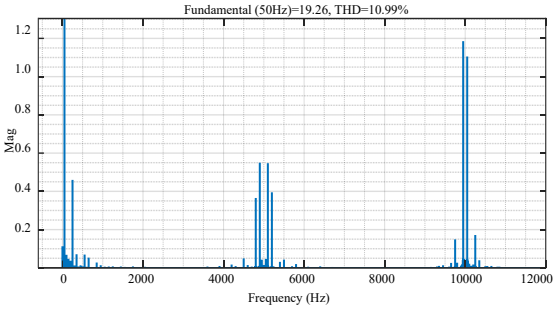


Fig. 25. Experimental results for ZSI. a) DC-link voltage, and Input current, b) capacitor voltage, c) Zooming of DC-link voltage, d) Zooming of input current, e) Zooming of load current with two phase ac voltage, f) THD in current, g) THD in voltage.

## REFERENCES


[1] Ihab Jamal Al Essawy; Mahmoud F. Elmorshedy; Sherif M. Dabour; Essam M. Rashad; Md Rabiul Islam, "A Grid-Connected PV System Based on Z-source Inverter with Maximum Power Extraction," *2021 IEEE 6th ICCCA*, December 2021.

[2] Po XU, Xing ZHANG, Chong-wei ZHANG Ren-xian, CAO and Liuchen CHANG, "Study of Z-source inverter for grid-connected PV systems," 2006 37th IEEE Power Electronics Specialists Conference, 2006.

[3] F. Z. Peng, "Z-source inverter," *IEEE Transactions on Industry Applications*, vol. 39, No. 2, pp. 504-510, March/April 2003.

[4] Y. Huang; M. Shen; F. Z. Peng; J. Wang, "A Z-source inverter for residential PV systems," *IEEE Transaction on Power Electronics*, vol. 21, no. 6, pp. 1776-1782, Nov. 2006.

[5] J. Chen, W. Yao, C.-K. Zhang, Y. Ren, and L. Jiang, "Design of robust MPPT controller for grid-connected PMSG-based wind turbine via perturbation observation-based nonlinear adaptive control," *Renewable Energy*, vol. 134, pp. 478-495, 2019.

[6] M. N. Uddin and I. K. Amin, "Adaptive step size-based hill-climb search algorithm for MPPT control of DFIG-WECS with reduced power fluctuation and improved tracking performance," *Electric Power Components and Systems*, pp. 1-15, 2019.

[7] O. Husev, T. Shults Dmitri Vinnikof, Carlos Ron cero-Clemente, "Comprehensive comparative impedance-source networks for DC and analysis of AC application," *Electronics*, 8, 405, Sep. 2019.

[8] Zhengyuan Zhao, Mohammed A. El Gendy, Matthew Armstrong, Musbahu Muhammad, "Constant boost control with third harmonic injection for quasi-Z source inverter used in PV grid-connected system," *IEEE catalog number: CFP19850-ART,* Mar. 2019.

[9] I. Boldea, L. N. Tutela, W. Xu, and M. Pucci, "Linear electric machines, drives, and MAGLEVs: an overview," *IEEE Trans. Ind. Electron.,* vol. 65, no. 9, pp. 7504-7515, Sept. 2018.

[10] V. R. Chowdhury and J. Kimball, "Adaptive feedback linearization-based control of a three-phase grid connected inverter under non-ideal grid voltage condition," *in Proc. Power and Energy Conference at Illinois (PECI)*, Feb 2019.

[11] M. Chuang, Li Hong, "Research on PV grid-connected control of Z source inverter based on active disturbance rejection technology," *IEEE 4th Advanced Information Technology, Electronic and Automation Control Conference (IAEAC*), Dec. 2019.

[12] Salman Ahmad1, Rahim Uddin, Zahoor Ahmad Ghanim, Aisha Tasneem "Closed loop control of quasi-Z-source inverter in grid-connected PV system," *IEEE*, 2019.

[13] Yam P. Siwakot, Fang Zheng Peng, Freda Blaabjerg, Poh Chiang Loh, and Graham E. Town, "Impedance-source networks for electric power conversion part I: A topological review," *IEEE Trans. Power Electronics,* Vol. 30, Issue: 2, Feb. 2015.

[14] Sitbon, M., Leppäaho, J., Suntio, T., Kuperman, A., "Dynamics of PV-generator-interfacing voltage-controlled buck power stage,*" IEEE J. Photovolt. 2015, 5, 633–640.*

[15] N. E. Zak zouk, "Mitigation of oscillating power effect on PV power and grid current in single-phase single-stage PV grid-tied systems," *7th Inter. Conference on Renewable Energy Research and Applications, CT.* 2018.

[16] Nafis Subhani, Ramani Kannan, M.d Apel Mahmud, and Fakhizan Romlie, "Performance analysis of a modernized Z-source inverter for robust boost control in PV power conditioning systems," *Electronics 2019*, no. 8, Vol. 139, Apr. 2019.

[17] Arvind Yadav, Subhash Chandra, Vinay Deolia, Sanjay Agrawal., "Z Source Inverter Application and Control for Decentralized PV System," *2017 3rd International Conference on Condition Assessment Techniques in Electrical Systems (CATCON)Proceedings for USB Distribution;* Part No. CFP1720V-USB; ISBN: 978-1-5386-3137-9 48, Nov. 2017.

[18] M. R. Nikzad, B. Asaei and S. O. Ahmadi, "Discrete duty-cycle-control method for direct torque control of induction motor drives with model predictive solution," *IEEE Trans. Power Electron.,* vol. 33, no. 3, pp. 2317-2329, Mar. 2018.

[19] Liu, W.; Yang, Y.; Kerekes, T.; Liivik, E.; Blaabjerg, F. "Impedance network impact on the controller design of the QZSI for PV applications,". *In Proceedings of the 2020 IEEE 21st Workshop on COMPEL, Aalborg, Denmark,* no. 9, vol. 12; pp. 1–6, November 2020.

[20] S. A. Davari, "Predictive direct angle control of induction motor," *IEEE Trans. Ind. Electron.,* vol. 63, no. 8, pp. 5276-5284, Aug. 2016.

[21] Oliveira-Assis, L.; Soares-Ramos, E.P.P.; Sarrias-Mena, R.; García-Triviño, P.; Fernández-Ramírez, L.M. "Large-scale grid connected quasi-Z-source inverter-based PV power plant,". *2020 EEEIC/I&CPS Europe, Madrid, Spain,* pp. 1–6, no. 9, vol. 12 June 2020.

[22] K. H. Ahmed, S. J. Finney and B. W. Williams, "Passive Filter Design for Three-Phase Inverter Interfacing in Distributed Generation," *2007 Compatibility in Power Electronics*, Gdansk, Poland, 2007, pp. 1-9.

[23] G. L. Calzo, A. Lidozzi, L. Solero and F. Crescimbini, "LC filter design for on-grid and off-grid distributed generating units," *2013 IEEE Energy Conversion Congress and Exposition*, Denver, CO, USA, 2013, pp. 713-720.

[24] J. M.-K. Nguyen, T.-D. Duong, Y.-C. Lim, J.-H. Choi, D. M. Vila thgamuwa, and G. R. Walker, "DC-link quasi-switched boost inverter with improved PWM strategy and its comparative evaluation," *IEEE Access,* vol. 8, pp. 53857-53867, 2020.

**Mahmoud F. Elmorshedy** (Member, IEEE) was born in Gharbeya, Egypt, in 1989. He received the B.Sc. and M.Sc. degrees in electrical engineering from Tanta University, Egypt, in 2012 and 2016, respectively, and the Ph.D. degree in electrical engineering from the School of Electrical and Electronic Engineering, Huazhong University of Science and Technology, China, in 2020. He started working as a Teaching Assistant with the Department of Electrical Power and Machines Engineering, Faculty of Engineering, Tanta University, in 2013, where he was promoted to an Assistant Lecturer, in June 2016. He is currently working as an Assistant Professor with the Department of Electrical Power and Machines Engineering, Faculty of Engineering, Tanta University. His research interests include linear induction motor, predictive control, power electronics, and renewable energy.

**Ehab Gamal Ali** was born in 1978 in Kafrelsheikh, Egypt. He obtained his B.Sc. in Electrical Engineering from Higher Technology Institute on the 10th of Ramadan and later completed his MSc in Electrical Power Engineering from Tanta University in 2022.

Ehab began his career as an Electrical Engineer at Tawam United Enterprise in 2003, where his dedication and hard work led him to climb the corporate ladder and ultimately attain the position of Department Manager. He is renowned for his expertise in control systems, power electronics, and renewable energy, which have been the focal points of his research interests.

**Sherif M. Dabour** (Senior Member of IEEE) received his BSc from Zagazig University, Egypt in 2002, and his MSc and PhD from Tanta University, Egypt in 2012 and 2015, respectively, all in Electrical Power Engineering. He is an Associate Professor (on academic leave) at Tanta University, Egypt, and currently works as a Researcher at Glasgow Caledonian University, UK. Dr. Dabour has an impressive publication record with over 60 international journal and conference papers, and has contributed to various research projects funded by prestigious organizations such as the European Commission, the Egyptian Academy of Scientific Research and Technology, and the Qatar National Research Foundation. His work has significantly advanced power electronics, and his expertise has been recognized by esteemed organizations. In recognition of his outstanding contributions to the field, he was endorsed as a Global Talent researcher on power electronics by the UK Royal Academy of Engineering. Furthermore, Sherif served as the Treasurer of the IEEE Power Electronics Society (PELS) Egypt chapter from 2017 to 2020 and is a reviewer for multiple journals, including IEEE Transactions on Power Electronics and Industrial Electronics, IET Power Applications, and IET Power Electronics.

**ESSAM M. RASHAD** (Senior Member, IEEE) was born in Shebin El-Kom, Egypt, in 1960. He received the B.Sc. degree from the Department of Electric Power and Machines Engineering, Faculty of Engineering, Menoufia University, Egypt, in 1983, and the M.Sc. and Ph.D. degrees from the Faculty of Engineering, Alexandria University, Egypt, in 1987 and 1992, respectively. From 1985 to 1990, he was an Offshore Electrical Engineer with Belayim Petroleum Company, Egypt. In 1992, he joined the Faculty of Engineering, Tanta University, Egypt, where he has been a Full Professor, since 2006. From February 2000 to August 2000, he was a Visiting Researcher with the Faculty of Engineering, Nagasaki University, Japan. In summer 2003, he was a Visiting Researcher with the Faculty of Engineering and Applied Science, Memorial University of Newfoundland, St. John's, Canada. From 2004 to 2009, he was the Head of the Electrical Technology Department, Buraydah College of Technology, Saudi Arabia. From 2011 to 2014, he was the Vice Dean for education and student affairs of the Faculty of Engineering, Tanta University. He was the Head of electrical power and machines engineering, from 2009 to 2011, and from 2014 to September 2020. He has published more than 160 technical conference and journal papers. His research interests include electrical machine analysis and design, electrical drives, power electronics, micro-grids, distributed generation, and renewable energy systems. Prof. Rashad received the Outstanding Engineering Award for ''Outstanding Contribution in the Electrical Power Engineering Education, Research and Industry'' from IEEE-PES (Power and Energy Society), Egypt Chapter, in 2019. He was the General Chairman of the 21st International Middle East Power Systems Conference (MEPCON'2019), Cairo, in December 2019, and the Co-Chairman of the First IEEE Conference on Power Electronics and Renewable Energy, Aswan, Egypt, in October 2019.